Impact of Acetic Acid Exposure on Metal Contact Degradation of Different Crystalline Silicon Solar Cell Technologies

Nafis Iqbal[a,b,1], Mengjie Li[a,b,c], Tamil S. Sakthivel[a,d], Kurt Mikeska[e], Meijun Lu[e], Naomi Nandakumar[f], Shubham Duttagupta[f], Marwan Dhamrin[g,h], Kosuke Tsuji[g], Stuart Bowden[i], André Augusto[i], Yuejun Guan[j], Sudipta Seal[a,d], Kristopher O. Davis[a,b,c,k,1]

[a] *Department of Materials Science and Engineering, University of Central Florida, Orlando, Florida, USA*
[b] *Resilient Intelligent Sustainable Energy Systems (RISES) Faculty Cluster, University of Central Florida, Orlando, Florida, USA*
[c] *FSEC Energy Research Center, Cocoa, Florida, USA*
[d] *Advanced Materials Processing and Analysis Center, NanoScience and Technology Center, University of Central Florida, Orlando, Florida, USA*
[e] *Research and Development Department, Jiangxi Jiayin Science and Technology, Ltd., Jiangxi, China*
[f] *Solar Energy Research Institute of Singapore (SERIS), National University of Singapore, Singapore*
[g] *Toyo Aluminium K.K., Shiga, Japan*
[h] *Graduate School of Engineering, Osaka University, Osaka, Japan*
[i] *School of Electrical, Computing and Energy Engineering, Arizona State University, Tempe, Arizona, USA*
[j] *Department of Electrical and Computer Engineering, University of Central Florida, Orlando, Florida, USA*
[k] *College of Optics and Photonics, University of Central Florida, Orlando, Florida, USA*

Abstract

Degradation due to acetic acid in photovoltaic (PV) modules has been a commonly observed phenomenon for both damp-heat exposure and outdoor operations. Acetic acid is a degradation byproduct of ethylene-vinyl acetate (EVA), a common module encapsulant. To address this issue, robust metallization pastes and cell technologies are being developed. However, it is important to assess how these technologies perform in an acetic acid environment and withstand degradation before they are implemented in the solar market. In this work, we investigate the impact of acetic acid exposure

on four different cell groups: monofacial passivated emitter and rear contact (PERC) cells with advanced telluride-based front contact pastes, bifacial PERC cells with novel aluminum rear contact pastes, bifacial tunnel oxide passivated contacts (TOPCon) cells, and silicon heterojunction (SHJ) cells. These cells were exposed to acetic acid for different time increments. The recombination losses were characterized by Suns-V_{OC}, and multi-variate regression analysis of intensity-dependent photoluminescence (PL) images with Griddler AI. Resistive losses were tracked with the transmission line method (TLM). Samples showing severe performance degradation were selected for further materials characterization to understand the root cause. Top-down and cross-sectional scanning electron microscopy (SEM), energy dispersive spectroscopy (EDS), and X-ray photoelectron spectroscopy (XPS) were performed to investigate the change in materials properties. Our study shows that the front contacts of the bifacial TOPCon cells and monofacial PERC cells were significantly affected by acetic acid exposure. The SHJ cells were found to be the most stable.

Keywords: Crystalline silicon solar cells, metallization paste, acetic acid, contact degradation, corrosion

---

1. Introduction

Photovoltaic (PV) researchers and manufacturers are constantly developing new cell and metallization technologies that allow for higher efficiencies [1, 2, 3]. This new generation of cell and metallization technologies are particularly attractive because of reasons such as reduced silver (Ag) usage, easier processing, lower performance losses, and better power output. However, factors like reliability and durability need to be evaluated before field deployment. A slight change in the cell architecture and/or the metal paste composition can vastly impact performance degradation in the field [4, 5]. One of the most commonly observed degradation mechanisms, both in the field and from accelerated aging tests like damp-heat (DH), is the corrosion of metal contacts due to acetic acid formation [6, 7, 8, 9, 10, 11, 12, 13, 14]. Acetic acid is formed as a decomposition product of ethylene-vinyl acetate (EVA), a common module encapsulation material [15, 16, 17, 18]. It interacts with the metallization, often causing degradation at the interface between the front metal contacts and underlying silicon (Si) substrate. This results in a loss of cell performance and contact adhesion, increased contact resistance,

and dark areas seen in electroluminescence (EL) imaging. Although other encapsulant materials are being explored to replace EVA and minimize this problem, nearly 80% of the current PV modules are encapsulated using EVA. This is because of the many advantages of EVA such as low-cost, good light transmittance, high elasticity, low processing temperature, excellent melt fluidity, and high adhesion, which makes it an attractive encapsulant for the solar industry [19].

In order to address the degradation issue, there have been efforts to change the EVA chemistry, and incorporate additives to minimize degradation [19]. Also, novel metallization pastes are being developed to be more resistant to acetic acid. For many years now, screen printing has been the preferred metallization approach in the industry due to its robust, simple, highly automated process, and the rapid developments in paste chemistries. However, early generation Ag screen printable pastes contained inorganic frits based on lead-silicate (Pb-Si-O) chemistries that have been reported to easily react with acetic acid, resulting in significant performance loss [16, 17]. New paste chemistries are being developed that both lower contact recombination and resistivity losses, as well as hopefully help withstand acetic acid degradation. In case of aluminum back surface field (Al-BSF) and passivated emitter and rear contact (PERC) cells [20, 21], novel screen-printable Ag pastes featuring lead-tellurite (Pb-Te-O) and Pb-free tellurite (Te-O) based frit have been developed to contact the front n^+ emitter [22, 23]. Researchers are also focusing on the rear aluminum Al contact for bifacial PERC cells, especially producing metal pastes to improve the bulk conductivity without compromising on the durability [24, 25, 26, 27].

Silicon heterojunction (SHJ) cells have been of particular interest to the solar industry for many different reasons such as higher conversion efficiencies, low processing costs, and compatibility with very thin wafers [1, 28, 29]. However, there are far fewer studies on this topic [30, 31, 32]. Doped polycrystalline silicon (poly-Si) passivating contacts featuring a thin silicon oxide (SiO_x) have garnered significant attention in recent years. Tunnel oxide passivating contact (TOPCon) and poly-Si on oxide (POLO) cells been shown to yield higher efficiencies due to a reduction in contact recombination without dramatically increasing the contact resistivity [33, 34, 35, 36]. These cells have much better thermal stability at higher temperatures, making them more compatible with the current industrial processes. However, very little is known about their reliability, stability, and long-term durability [37].

In this work, we investigate the impact of acetic acid exposure on novel

solar cell technologies, and metallization techniques. The technologies investigated in this work are monofacial PERC with advanced telluride (Te)-based pastes, bifacial PERC with novel rear Al pastes, bifacial TOPCon cells, and SHJ cells. Industrial solar cells were exposed to acetic acid for different time increments. A subset of the cells were also exposed to pure water to establish a baseline and compare the impact. Different optical and optoelectrical characterizations were performed at each step of exposure. Materials characterization was performed on selected samples to fully understand the change in materials properties. This multiscale characterization procedure allows for a direct approach to understanding the impact of acetic acid on different cell and metallization technologies.

2. Experiment

In this work, four different cell types, each with different groups, were studied. The cell architectures for each of the cell types are shown in Figure 1 and the key differences within the groups for each cell type is listed in Table 1. The first cell type are the monofacial PERC cells with advanced Te-based front contact pastes. Commercially available p-type, front junction, pseudo square Cz-Si wafers with a bulk resistivity of 2 Ω·cm were used with 100-110 Ω/sq. phosphorus emitter, 75 nm thick plasma-enhanced chemical vapor deposition (PECVD) SiN_x:H ARC on the front and an atomic layer deposition (ALD) Al_2O_3 rear surface passivation. The front H-grid pattern was a 5-busbar design with two sets of circular transmission line method (cTLM) structures [38] and the rear side of the cells features local contact opening and full area Al printing. For G1, a Pb-Te-O-based Ag screen-printing paste was used for front metallization. For G2, Pb-free Te-O-based Ag screen-printing paste was used. The second cell type are commercially available bifacial PERC cells. This group had a traditional Ag front contact paste. There are four groups with different Al-based rear contact pastes. G1 had a standard industrial Al PERC rear contact paste. The G2, G3, and G4 had Al pastes containing boron (B) family of oxides, bismuth (Bi) family of oxides, and vanadium (V) family of oxides respectively as additives. The back contacts had an H-pattern grid design with a 30 μm laser opening to form local contacts. The next cell type is the bifacial TOPCon. These samples used a Ag-Al-based fire through front contact paste to contact the B-doped p^+ front emitter, and a Ag-based fire through rear contact paste to contact the rear poly-Si (n^+) based passivating carrier selective contact.

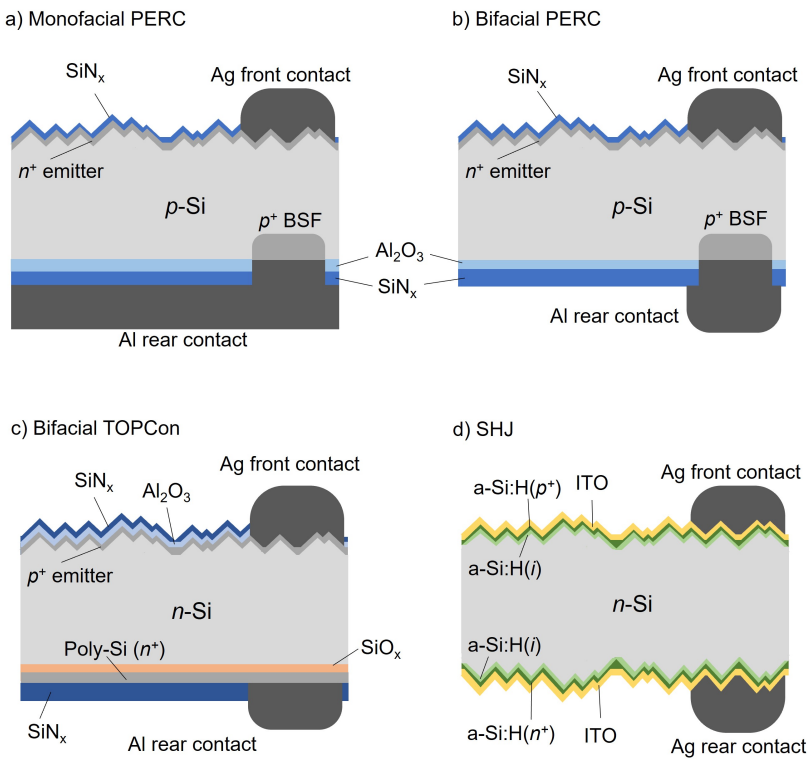

Figure 1: Schematic illustration of the cell architectures investigated in this experiment.

Group G1 had a base wafer thickness of 150 μm and G2 had a base wafer thickness of 115 μm. The last cell group is the SHJ with a 3 busbar H-pattern design with Ag front contact and full area Ag rear contact.

Full cells and transmission line method (TLM) strips were exposed to aqueous acetic acid solutions for 30, 60, 90, and 120 minutes. We chose an acetic acid concentration of ≈5 vol.% (0.84M) based on previous reports of acetic acid concentration found in the field and DH-exposed modules [15, 17, 39, 40, 32]. A subset of the samples was also exposed to DI water for 120 minutes to establish an exposure baseline and compare the effect of pure water on performance. A diagram of our treatment setup is shown in Figure 2.

All the control and exposed samples went through a sequence of characterization techniques. Suns-V_{OC} [41] and intensity-dependent photoluminescence (PL) imaging followed by multivariate regression analysis with Griddler

Table 1: List of cell types with key differences among the groups.

Cell Type	Group	Front Contact Paste	Rear Contact Paste	Remarks
Monofacial PERC	G1	Pb-Te-O based	Al (full area)	Novel Te based front contact paste
	G2	Pb-free Te-O based	Al (full area)	
Bifacial PERC	G1	Ag	Al (H-pattern)	Standard rear Al paste
	G2	Ag	Al (H-pattern)	B family of oxides
	G3	Ag	Al (H-pattern)	Bi family of oxides
	G4	Ag	Al (H-pattern)	V family of oxides
Bifacial TOPCon	G1	Ag-Al	Ag (H-pattern)	Difference in wafer thickness
	G2	Ag-Al	Ag (H-pattern)	
SHJ	G1	Ag	Ag (full area)	Low temperature Ag pastes

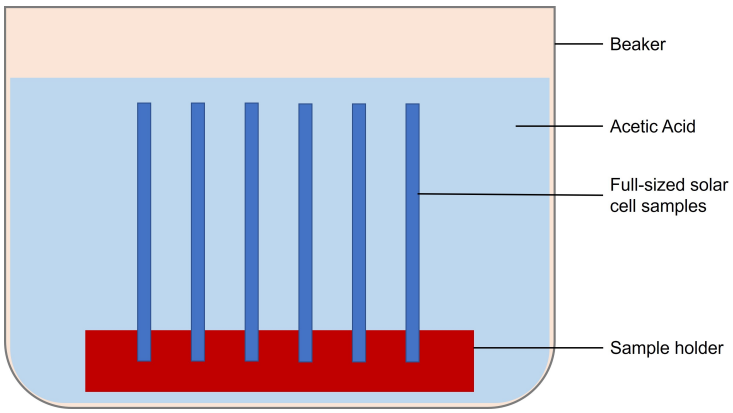

Figure 2: Schematic illustration of the acid and water treatment setup used in this experiment for full sized solar cells and TLM strips.

AI [42, 43] were used to analyze the recombination losses. A BT Imaging LIS-R1 photoluminescence (PL) system was used in this work, featuring an 808 nm wavelength laser as the excitation source. The emitted PL signal was captured by a 1-megapixel Si charge-coupled device (CCD) camera with a 920 nm long-pass filter. A photon flux values of 3.085×10^{17} $cm^{-2}s^{-1}$ was assumed to be 1 sun, which was determined by calibrating the photon flux value towards matching the short-circuit current density (J_{SC}) of a reference solar cell with known EQE data [43, 44]. TLM and cTLM measurements were performed to measure the changes in contact resistivity [38, 45]. TLM strips were prepared from full cells using a laser scribe and cleave method. Contact recombination and contact resistivity analysis were performed for all the front contacts. As for the rear, only bifacial cells were measured since the accurate quantification of the contact recombination losses or the measurement of contact resistivity can be challenging for full area rear contacts. All of these measurements were repeated after each exposure step.

Samples that show severe performance losses were selected for further materials characterization. Top-down scanning electron microscopy (SEM) imaging and energy dispersive spectroscopy (EDS) analyses were performed on the control and degraded contacts using a ZEISS Ultra 55 SEM. An acceleration voltage of 3 kV, a working distance of 5 mm, and a secondary electron (SE) detector were used to capture the images. EDS analysis was performed using an acceleration voltage of 30 kV, a working distance of 13 mm, and the EDS detector. ZEISS SmartSEM software was used to collect and analyze the SEM images and EDS data. X-ray photoelectron spectroscopy (XPS) analysis was performed on top of these contacts to further investigate the compositional changes after exposure. A Thermo Scientific ESCALAB-250Xi spectrometer in an ultra-high vacuum (UHV) chamber (below 7×10^{-9} mbar). An Al-K_α monochromatic radiation source (binding energy 1486 eV) was used, operating at a power of 300 W (15 kV, 20 mA). The spot size of the X-ray was 200 μm and C 1s peak at 284.8 eV was used as a base for calibration within an experimental error of $\pm$ 0.2 eV. A Thermo Scientific Avatange Data System software was used to record and analyze (processing, deconvolution, peak fitting and atomic % quantification) the data. The uncertainty in the peak fitting spectra is in the order of $\pm$ 0.4 eV [18]. Samples that needed further investigation were prepared for cross-sectional analysis. Cross-sectional samples were first prepared using a TYKMA Minilase industrial system. Next, ion milling was performed on the samples using an FEI FIB 200 system to clean the laser damage and make a flat surface for cross-

sectional microscopy. Approximately 10 μm from the cross-section edge was milled out to rule out any possible laser damage or peel-off due to sample preparation. Finally, SEM imaging with backscattered electron (BSE) detector, and EDS analyses were performed on the cross-sections using the ZEISS Ultra 55 SEM.

3. Results and Discussion

The results from the different characterization techniques show that the extent of degradation due to acid and water exposure varies largely within the different groups. An example of the variation due to acetic acid exposure for different cells can be found in the open-circuit PL images shown in supplementary information S1.

Figure 3 shows a comparison of the cell level open-circuit voltage (V_{OC}), and saturation current density (J_0) obtained from Suns-V_{OC} measurements. With the exposure to acetic acid, there is a drop in cell V_{OC}, and a corresponding increase in cell J_0 which is an indication of recombination losses. A comparison between the two monofacial PERC cells shows G2, which is the Pb-free Te-O-based paste, degrades more than G1, which is Pb-Te-O-based paste. The bifacial PERC cell group with four different pastes also show some degradation. However, the extent of degradation is less compared to the monofacial PERC group. Among the bifacial PERC cells, G4 with a new generation of rear Al paste containing vanadium family of oxides as additives seems to have degraded slightly more than the others. Bifacial TOPCon cells which have significantly better performance than the other two cell types initially seem to be stable and only show slight V_{OC} and J_0 degradation. Interestingly, although the samples are processed exactly in the same way, G2 is more stable than G1. The best performer are the SHJ cells. Not only do they have the highest V_{OC}, but they also seem to have the least amount of degradation due to acid exposure. The water exposure results are also shown. All the cell groups seem to be stable in water with some showing very minor degradation. This is an indication that water (which is a representation of moisture in this experiment) alone would not affect cell performance at room temperature.

To further investigate performance degradation, we quantified the contact recombination losses ($J_{0\mathrm{c}}$) by obtaining PL images at multiple illuminations and conditions followed by analyzing the images using Griddler AI. A detail discussion about the method can be found in [42, 46]. The extracted values

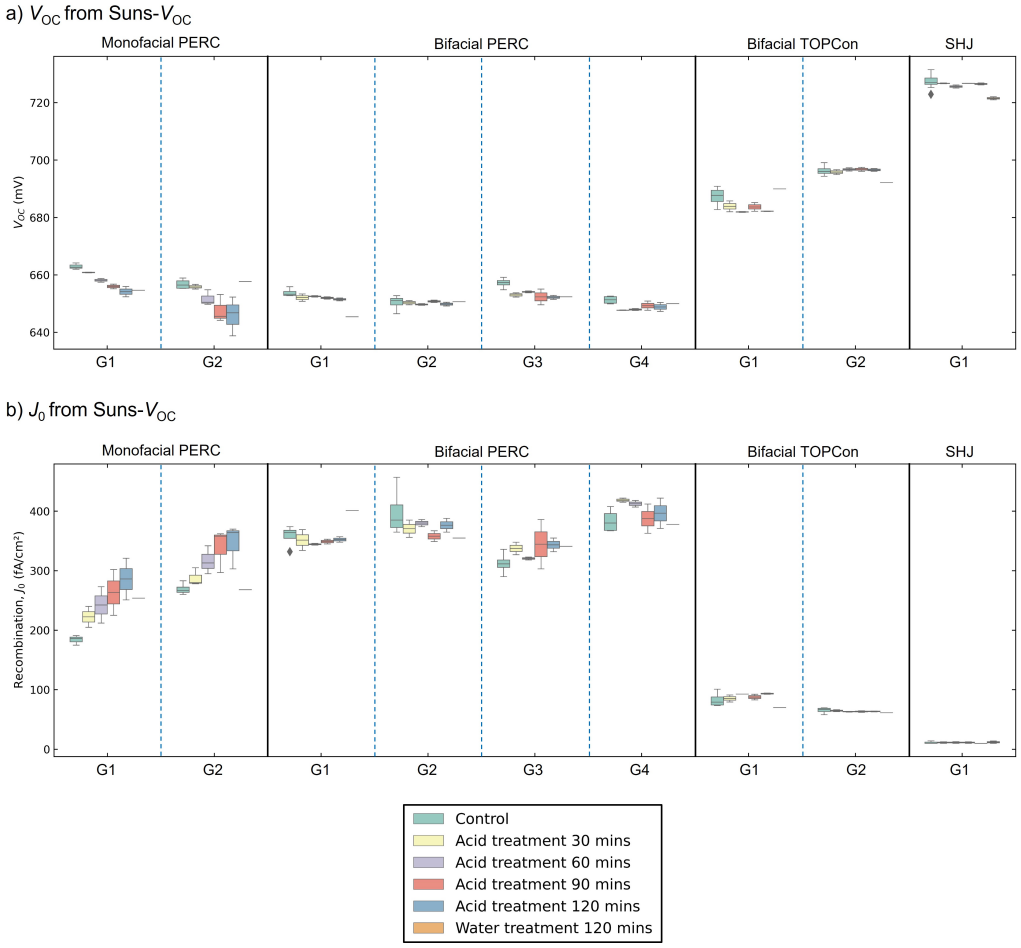

Figure 3: Comparison of cell V_{OC} (a) and cell J_0 (b) obtained from Suns-V_{OC} measurements. Measurement results from each exposure step is shown for comparison.

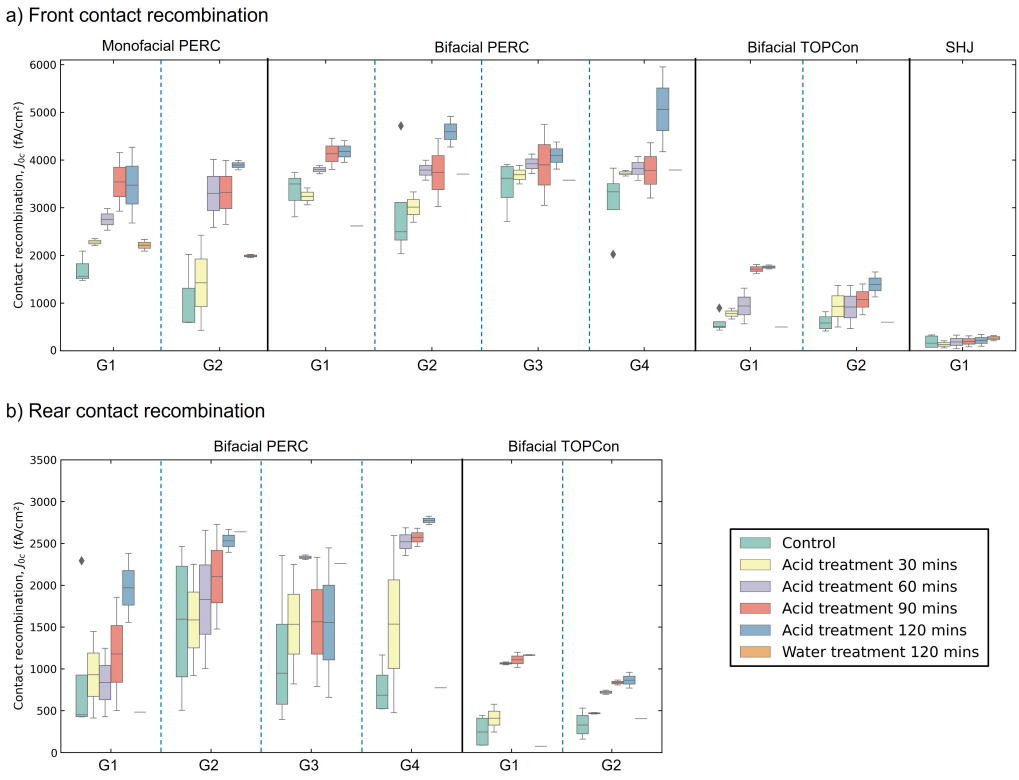

Figure 4: Front J_{0c} (a) and rear J_{0c} (b) extracted from intensity dependent PL images and Griddler AI analysis. Results for controls, and each exposure step are shown for comparison.

for both front J_{0c} (a) and rear J_{0c} (for bifacial cells) (b) are shown in Figure 4. For the front J_{0c} shown in Figure 4(a), the G2 monofacial PERC cells (with Pb-free Te-O based paste) have a lower J_{0c} loss compared to the G1 (Pb-Te-O based paste) cells. However, they both see similar levels of degradation after acid exposure. All the bifacial PERC cell groups have a similar initial J_{0c}. This is because they have the same Ag front contact paste. The degradation due to acid exposure is also similar among the groups which is expected. Both the bifacial TOPCon groups also behave similarly throughout the acetic acid exposure. The most interesting result is seen for the SHJ cells, which seem to have been affected the least due to acid treatment. This trend is in agreement with the Suns-V_{OC} results shown previously. For the rear J_{0c} shown in Figure 4(b), the bifacial PERC cells show some variation in the initial J_{0c} values. This is due to the slight difference in composition of the Al rear contact paste. After acid treatment, they all reach a similar level of degradation. However, if we take a look at each step, we see a varying level of degradation. This could be due to the difference in additives, which influences the acetic acid stability of the Al contacts. Among the bifacial TOPCon cells, G1 has slightly higher levels of rear J_{0c} degradation compared to G2. Most of the cell groups do not show a significant amount of contact degradation due to water exposure, except for a few which show a very minor change. This result is in agreement with the Suns-V_{OC} data shown in the previous section.

Figure 5 shows the contact resistivity (ρ_c) data for all the control and exposed samples. These measurements were performed using the cTLM (for monofacial PERC) and TLM method. For the front ρ_c measurements shown in Figure 5(a), the G1 monofacial PERC (with the Pb-Te-O based paste) samples show lower initial ρ_c than the G2 samples (Pb-free Te-O based paste). After treatment, both the sample sets had an increase in ρ_c values. The G2 samples have a very high increase in ρ_c values. All the bifacial PERC groups have a similar initial ρ_c. They also show some degradation due to acid exposure with G4 samples degrading more than the others. The SHJ cell group does not show any degradation due to acid exposure. The most significant degradation is observed for both the bifacial TOPCon cells. Some of the samples show complete loss of contact after the final step of acid exposure. Others that made contact had a very high ρ_c as seen in the Figure 5(a). As for the water exposure, the monofiacial PERC samples show a slight increase in ρ_c. The rest of the samples did not show a significant increase in front ρ_c. The rear ρ_c results for the bifacial cells are shown in Figure

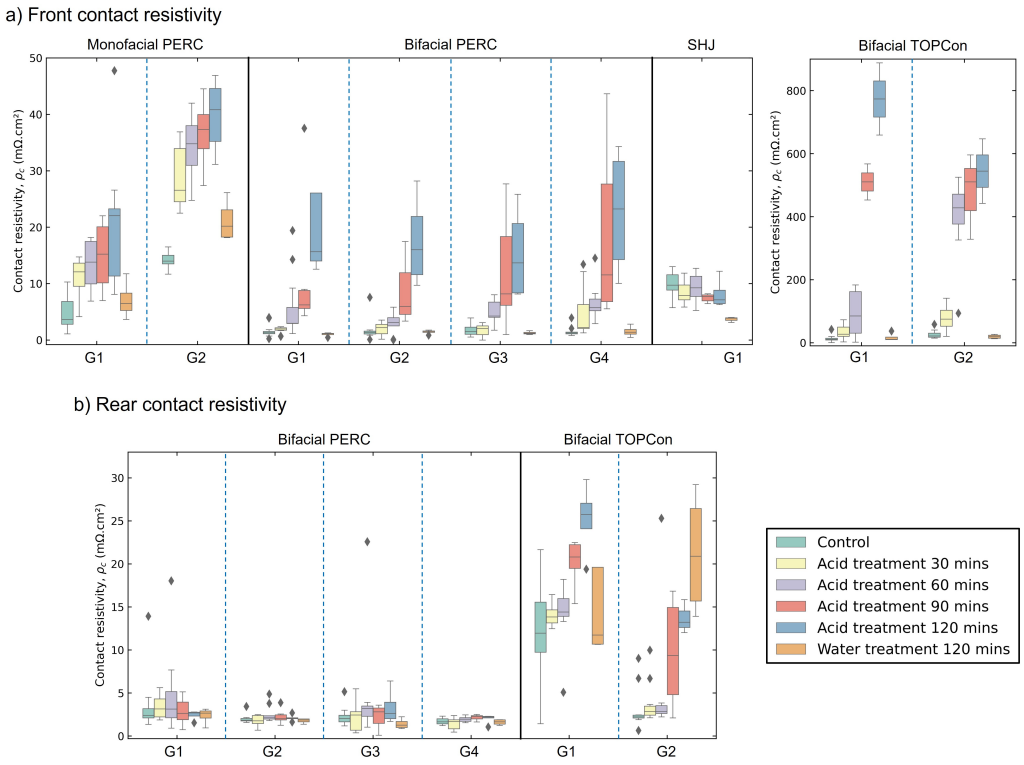

Figure 5: Contact resistivity (ρ_c) measurement results for the (a) front contacts, and (b) rear contacts. Results for controls, and each exposure step are shown for comparison.

5(b). The different bifacial PERC cell groups do not show any significant change due to acid or water exposure. However, the bifacial TOPCon shows an increase in ρ_c both for acid and water exposure.

A summary of the device characterization results is shown in supplementary information S2. The change (Δ) in cell parameters after 120 minutes of acetic acid and water treatment compared to controls (baseline) is shown.

To investigate the change in contact properties of the different groups further, materials characterizations were performed. Among the different cell types, the bifacial TOPCon shows the most degradation followed by the monofacial PERC for acetic acid exposure. Therefore, samples from these groups were selected for further investigation. Figure 6(a) shows top-down SEM and EDS analyses performed on the control and acid treated contacts of groups G1 and G2 monofacial PERC cells. After a visual inspection, it seems like for the G1 acid-treated sample, there is a dispersion of Ag that's taking place. Ag seems to be spread out near the busbar which is clearly seen in the EDS map. For the G2 sample, there is little dispersion of Ag. Instead, there are large chunks of Ag missing from the metallization observed in the center region of the SEM image and EDS map, exposing the underlying Si. This indicates that the Pb-free paste (G2) degrades more in acetic acid, and is likely the reason we see more performance degradation for the G2 group of cells. Further investigation is performed using the high-resolution XPS analysis shown in Figure 6(b). Looking at the monofacial PERC G1, it is observed that the Ag has changed due to acetic acid treatment. The control sample contains 96.6% metallic Ag, and 3.4% Ag^+ and the acid-treated sample contains 90.6% metallic Ag, and 9.4% Ag^+, which is an indication of Ag oxidation [18]. The intensity of the Ag peak was also decreased, which suggests changes/decomposition of the Ag. Furthermore, looking at the Pb 4f spectrum, Pb in the form of PbO was present in the control sample. However, for the acid-treated sample, PbO is almost non-existing. This is a clear sign of the Pb-elusion phenomenon seen in DH-induced/acetic acid degradation [16, 17, 18]. On the other hand, the monofacial PERC G2 samples show some interesting features. From the Ag 3d spectrum we see that the control sample contains 95.7% metallic Ag, and 4.3% Ag^+ and the acid-treated sample contains 95.8% metallic Ag, and 4.2% Ag^+, suggesting that the Ag is not strongly affected by acetic acid. The major change is seen in the Te 3d spectrum. For the control, Te is present in the form of TeO_2. There is a peak overlap of Te 3d with Ag 3p. The acid-treated samples show a change in the TeO_2 composition. There is a strong peak which could be attributed

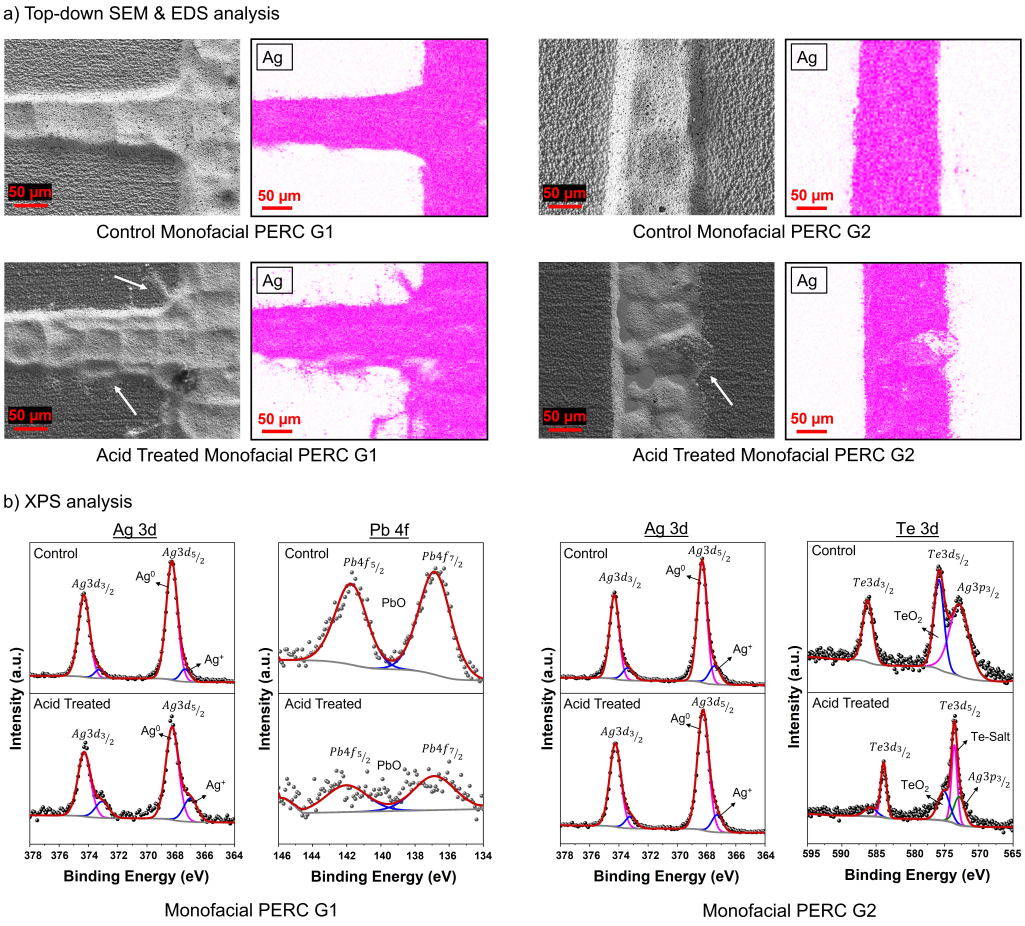

Figure 6: (a) Top-down SEM imaging and Ag EDS maps of the monofacial PERC G1 and G2 control and acetic acid treated contacts. (b) High-resolution Ag 3d, Pb 4f, and Te 3d spectrum of control and acid treated monofacial PERC G1 and G2 contacts.

a) Cross-sectional SEM

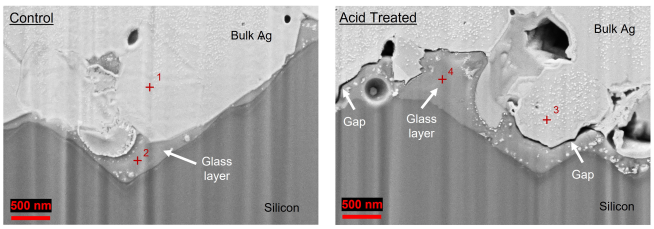

Monofacial PERC G2

b) EDS quantification

	Monofacial PERC G2			
	Control (Wt. %)		Acid Treated (Wt. %)	
Elements	P1	P2	P3	P4
Ag	78.5	58.4	72.5	51.3
Si	10.7	17.3	16.4	25.6
O	2.4	14.6	2.2	13.4
C	7.1	3.9	8.1	6.4
Te	1.3	2.6	0.8	1.2
Bi	--	2.3	--	1.3
Zn	--	0.9	--	0.8

Figure 7: Cross-sectional SEM imaging (a), and EDS quantification (b) for the control and acid treated monofacial PERC G2 contacts.

to Te-salt/compound [47], in addition to the TeO_2, which has also reduced in intensity. This suggests that TeO_2 is unstable in an acetic acid environment and changes composition, which might be a reason for the delamination and performance degradation.

Since the monofacial PERC G2 samples, containing the novel Pb-free Te-O-based paste, degraded more than the Pb-based paste, they were further investigated using cross-sectional SEM imaging and EDS analysis. Control and acid-treated samples were selected. Three contact areas per type were investigated along almost the entire contact width. Representative images with the key microstructural observations are shown in Figure 7(a). The key difference between the control and the acid-treated samples was the gap/delamination which formed between the bulk Ag and the interfacial glass layer in the acid-treated sample. This gap/delamination was very prominent throughout the entire cross-sections for all the acid-treated contacts investigated. The back-scattered electrons (BSE) images show very minor mass contrast differences in the interfacial glass layer. The metal delamination and significant performance loss could be attributed to this gap/delamination formation, which is creating a loss in electrical contact. EDS spectrum was obtained at a few different points both for the control and acid-treated contacts to look for compositional changes, as shown in 7(b). The key element for points 1 and 3, which were obtained on the bulk Ag of the control and acid-treated contacts, mainly is Ag with a little bit of Te. After the treatment, both Ag and Te contents seem to have dropped slightly, which signifies the decomposition of the contacts. Points 2 and 4 reports the composition of the glass layers. A somewhat significant drop in the Ag, Te, and Bi contents was

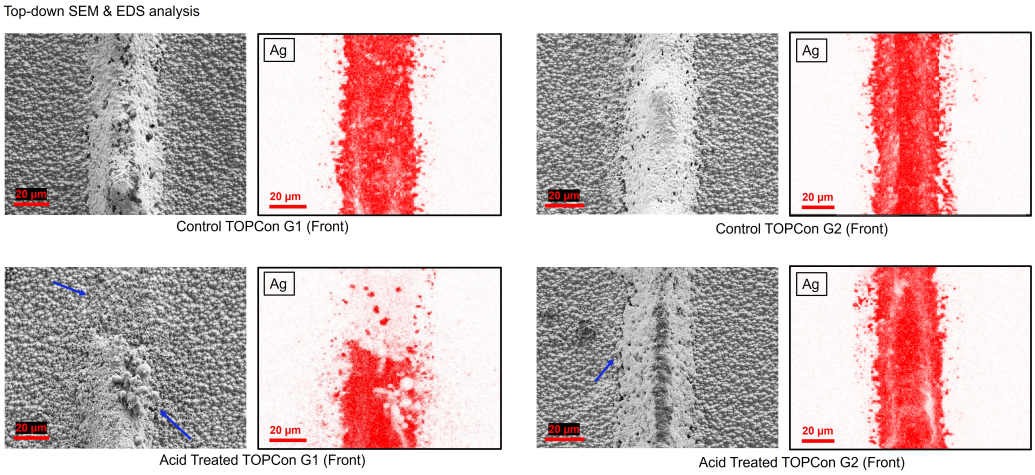

Figure 8: Top-down SEM imaging and Ag EDS maps of the control and acid treated bifacial TOPCon G1 and G2 front contacts.

seen for the acid-treated sample. The dissolution of these elements/oxides from the glass layer in acetic acid, could have resulted in the gap formation. Previous studies have only talked about Pb-elusion being the main reason for this kind of degradation. But even with contacts completely free of Pb, this elusion/degradation is seen, which suggests that other elements are also involved in acetic acid degradation.

The bifacial TOPCon cells were also investigated via materials characterization since this group has shown the highest degradation in cell parameters. Among the control, acid-treated, and water-treated front and back contacts of the G1 and G2 samples, only the acid-treated front G1 samples show severe delamination and peel-off. This is in agreement with the electrical characterization results shown previously. Representative SEM images and Ag EDS maps of the controls and acid treated samples are shown in Figure 8. For the acid-treated G1 front contacts, there were visible signs (blue arrows) of delamination and degradation of the contacts. This is also confirmed with EDS maps. On the other hand, the acid-treated G2 front contact shows minor visual signs of degradation. Both G1 and G2 have the exact same front metal paste composition. The only difference is the base wafer thickness. The difference in the extent of degradation could be due to the way the contacts are formed. The wafer thickness is known to affect the overall heat received

a) Cross-sectional SEM

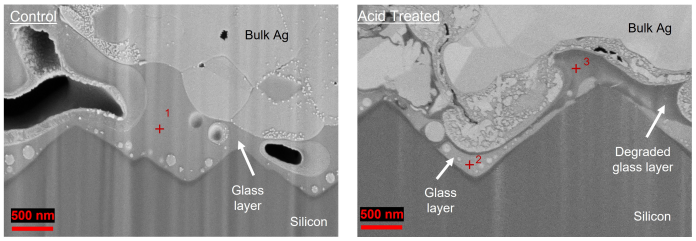

TOPCon G1 (Front)

b) EDS quantification

	TOPCon G1 (Front)		
	Control (Wt. %)	Acid Treated (Wt. %)	
Elements	P1	P2	P3
Ag	33.5	42.7	35.2
Si	24.9	28.2	38.4
O	9.7	7.7	17.8
C	2.8	2.7	3.6
Al	0.6	0.5	0.4
Pb	26.2	17.1	4.1
Zn	2.3	1.1	0.5

Figure 9: Cross-sectional SEM imaging (a), and EDS quantification (b) for the front side of the control and acid treated bifacial TOPCon G1 contacts.

by the interface during firing, resulting in potential differences in the final contact geometry, chemistry, and microstructure. We have seen examples of this in previous studies of Ag fingers contacting n^+ silicon surfaces [42, 38]. This difference could be the reason why acetic acid attacks the sample differently. Interestingly, this all pertains to the Ag-Al fingers that contact the p^+ front homojunction, and not the the rear Ag contacts contacting the newer poly-Si-based technology. The rear poly-Si does not appear to degrade severly, based on top-down SEM/EDS and electrical characterization. The results suggest potential concerns about TOPCon durability may not be centered around the poly-Si passivating contact, but rather the Ag-Al-based front contacts contacting the p^+ boron emitter. Lessons may therefore be learned from prior work on n-type cells featuring p^+n homojunctions and screen-printed, fire-through Ag-Al pastes [48].

Cross-sectional SEM imaging and EDS analysis were performed on the G1 samples to look at the change in the metal-Si interface/glass layer. BSE images were obtained to look at the mass contrast followed by EDS at different points. The cross-sectional SEM images and EDS maps for the control and acid-treated G1 front contact is shown are Figure 9(a). The control sample shows a very uniform contrast for the glass layer with no gaps between the bulk Ag and the glass layer. The acid-treated sample, on the other hand, also does not show any gap. However, there is a contrast difference in the glass layer in the BSE image which was very prominent. Different points were selected within the glass layers to investigate the compositional changes as shown in Figure 9(b). Point 1 and point 2 compares the control and bright region of the acid-treated samples respectively. The composition

Table 2: List of the main degradation mode and acetic acid durability/susceptibility for different cell types.

Cell Type	Group	Primary Degradation Mode	Durability/Susceptibility
Monofacial PERC	G1	Increase in resistance and recombination losses due to Ag finger degradation	Susceptible
	G2	Increase in resistance and recombination losses due to Ag finger degradation	Susceptible
Bifacial PERC	G1	Increase in resistance losses	Durable
	G2	Increase in resistance losses	Susceptible
	G3	Increase in resistance losses	Durable
	G4	Increase in resistance losses and recombination losses	Susceptible
Bifacial TOPCon	G1	Increase in resistance losses due to front Ag finger degradation	Most Susceptible
	G2	Increase in resistance losses due to front Ag finger degradation	Most Susceptible
SHJ	G1	No significant degradation	Most Durable

seems to be similar except for Pb, Zn, and Al which is slightly lower than the control. Point 3 shows quantification for the dark region of the acid-treated glass layer. Compared to the previous two points, the Pb and Zn content is significantly lower. The decreasing Pb content in the glass layer is a signature of Pb-elusion due to acetic acid degradation. Furthermore, the Zn content is also decreasing. Zn/ZnO is known to provide denser microstructure, better adhesion, and wetting ability resulting in superior electrical performance of the contacts [49, 50]. Therefore, it is natural that the decreased Zn content will not only result in bad contact performance as seen in the previous sections, but it will result in delamination [51]. This could be the most likely reason for the degradation observed in the TOPCon G1 front contact.

4. Conclusion

The different cell groups in this study behave differently when exposed to acetic acid. A summary of the main degradation mode and acetic acid durability/susceptibility for different cell types is shown in Table 2. The monofacial PERC cells have been metalized with novel screen-printable Te-based pastes. The initial performance for the Pb-based paste seems to be better than the Pb-free paste. After exposure, both the groups degrade significantly. We see an increase in both the ρ_c and J_{0c} after acetic acid exposure. This could be because acetic acid attacks the glass layer/metal-Si interface, which not only offers electrical conductivity but also helps passivate the contact region. Therefore, it is natural to see such degradation in performance.

Further materials characterization revealed how differently the contacts behave in an acid environment. Although previous studies have suggested that Pb is the main reason for acetic acid degradation and gap formation, it is interesting to see that the Pb-free Te-based paste in our study degrades more than the Pb-based paste both in terms of performance and geometry. This strongly suggests that other elements such as Bi, Zn, Te, and Ag in the glass layer also get attacked by acetic acid which contributes to the degradation.

The bifacial PERC cells with different novel Al pastes show very stable performance throughout the experiment. For all four groups, the control samples show a very similar performance. After acid treatment, Groups G1 (with standard Al paste) and G3 (with bismuth family of oxides) show slightly stable performance. G2 (with boron family of oxides) and G4 (with vanadium family) of oxides have a little more degradation than the others. Especially, the G4 samples have the worst performance both in acid and water. The front contact resistance and recombination degradation were pretty much similar since they were the exact same pastes, which is a standard Pb-Te-O-based paste. Very interestingly, the back contact resistance degradation is very minor although the pastes were different. This is expected because there is no glass layer for the rear contacts. The Al-Si eutectic (BSF) formed in the back contact interface is very stable and is not affected by acid or water.

The bifacial TOPCon groups G1 and G2 samples were processed exactly the same way, the only difference being the wafer thickness. Interestingly, these samples show very significant amount of degradation in acetic acid which is mostly related to resistance issues. The front contacts were degraded to the point that some of the fingers did not have any electrical connections. The back contacts also show an increase in ρ_c. Note that, it is natural to think that the rear contacts, contacting the poly-Si, might have reliability issues due to being a newer technology. However, we see that it is the front side that is affected the most. The rear has a Ag-based fire through contacts which behaved like any other Ag front contacts with glass layers. It was also interesting to see that although the paste composition and processing conditions were exactly the same, G1 samples show much more degradation (both front and rear) compared to the G2 samples. Since the only difference was the wafer thickness, we think that the amount of heat received by the interface during firing has affected the way the contacts have formed both in composition/chemistry and geometry. This could be the reason why the contacts behave so differently in an acetic acid environment. Taking a deeper

look into the contact degradation, we see a very prominent degraded/dark region in the glass layer via cross-sectional SEM imaging. EDS analysis suggested that these degraded regions have significantly less amount of Pb and Zn. Apart from Pb-elusion, which is common for acetic acid degradation, there is Zn-elusion as well which could be one of the key reasons for adhesion losses and delamination.

The last and most stable of all the groups is the SHJ cells. SHJ has been in the industry for a while now. More recently, manufacturers are becoming more interested in SHJ due to its high efficiency gains. It was interesting to see very insignificant amounts of degradation due to acid and water treatment. SHJ samples use a low-temperature Ag paste that directly contacts the indium tin oxide (ITO). There is no glass layer in the Ag/ITO interface. Therefore, it is natural that acetic acid would not have a significant effect on their performance. We also did not see any recombination degradation, suggesting that the thin-film layers were not affected by acetic acid.

Acknowledgment

This material is based upon work supported by the U.S. Department of Energy's Office of Energy Efficiency and Renewable Energy (EERE) under the Solar Energy Technologies Office Agreement Number DE-EE0008155. The authors also acknowledge the NSF MRI: ECCS: 1726636 and MCF-AMPAC facility, MSE and CECS.

References

[1] C. Battaglia, A. Cuevas, S. De Wolf, High-efficiency crystalline silicon solar cells: status and perspectives, Energy & Environmental Science 9 (2016) 1552–1576. doi:10.1039/C5EE03380B.

[2] J. Liu, Y. Yao, S. Xiao, X. Gu, Review of status developments of high-efficiency crystalline silicon solar cells, Journal of Physics D: Applied Physics 51 (2018) 123001.

[3] M. A. Green, E. D. Dunlop, J. Hohl-Ebinger, M. Yoshita, N. Kopidakis, X. Hao, Solar cell efficiency tables (version 58), Progress in Photovoltaics: Research and Applications 29 (2021).

[4] D. Jordan, D. Kern, S. Johnston, H. Moutinho, C. S. Jiang, C. Xiao, A. Norman, C. Deline, I. Repins, R. Bhoopathy, et al., High Efficiency Silicon Module Degradation-From Atoms to Systems, Technical Report, National Renewable Energy Lab.(NREL), Golden, CO (United States), 2020.

[5] D. C. Jordan, B. Marion, C. Deline, T. Barnes, M. Bolinger, Pv field reliability status—analysis of 100 000 solar systems, Progress in Photovoltaics: Research and Applications 28 (2020) 739–754. doi:10.1002/pip.3262.

[6] K. O. Davis, M. P. Rodgers, G. Scardera, R. P. Brooker, H. Seigneur, N. Mohajeri, N. G. Dhere, J. Wohlgemuth, E. Schneller, N. Shiradkar, et al., Manufacturing metrology for c-si module reliability and durability part ii: Cell manufacturing, Renewable and Sustainable Energy Reviews 59 (2016) 225–252.

[7] D. C. Jordan, B. Sekulic, B. Marion, S. R. Kurtz, Performance and aging of a 20-year-old silicon pv system, IEEE Journal of Photovoltaics 5 (2015) 744–751. doi:10.1109/JPHOTOV.2015.2396360.

[8] E. J. Schneller, R. P. Brooker, N. S. Shiradkar, M. P. Rodgers, N. G. Dhere, K. O. Davis, H. P. Seigneur, N. Mohajeri, J. Wohlgemuth, G. Scardera, et al., Manufacturing metrology for c-si module reliability and durability part iii: Module manufacturing, Renewable and Sustainable Energy Reviews 59 (2016) 992–1016.

[9] Z. Liu, M. L. Castillo, A. Youssef, J. G. Serdy, A. Watts, C. Schmid, S. Kurtz, I. M. Peters, T. Buonassisi, Quantitative analysis of degradation mechanisms in 30-year-old pv modules, Solar Energy Materials and Solar Cells 200 (2019) 110019. doi:10.1016/j.solmat.2019.110019.

[10] A. Omazic, G. Oreski, M. Halwachs, G. Eder, C. Hirschl, L. Neumaier, G. Pinter, M. Erceg, Relation between degradation of polymeric components in crystalline silicon PV module and climatic conditions: A literature review, Solar Energy Materials and Solar Cells 192 (2019) 123–133. doi:10.1016/j.solmat.2018.12.027.

[11] M. Köntges, G. Oreski, U. Jahn, M. Herz, P. Hacke, K.-A. Weiß, Assessment of photovoltaic module failures in the field: International Energy Agency Photovoltaic Power Systems Programme: IEA PVPS Task

13, Subtask 3: report IEA-PVPS T13-09:2017, International Energy Agency, Paris, 2017.

[12] S. Yang, L. Jiang, Crystalline Silicon PV Module Field Failures, in: Durability and Reliability of Polymers and Other Materials in Photovoltaic Modules, Elsevier, 2019, pp. 177–216. doi:10.1016/B978-0-12-811545-9.00008-2.

[13] R. Dubey, S. Chattopadhyay, V. Kuthanazhi, A. Kottantharayil, C. Singh Solanki, B. M. Arora, K. L. Narasimhan, J. Vasi, B. Bora, Y. K. Singh, O. S. Sastry, Comprehensive study of performance degradation of field-mounted photovoltaic modules in India, Energy Science & Engineering 5 (2017) 51–64. doi:10.1002/ese3.150.

[14] K. Kato, PV module failures observed in the field, PV Module Reliability Workshop, Golden, CO (2012).

[15] M. D. Kempe, G. J. Jorgensen, K. M. Terwilliger, T. J. McMahon, C. E. Kennedy, T. T. Borek, Acetic acid production and glass transition concerns with ethylene-vinyl acetate used in photovoltaic devices, Solar energy materials and solar cells 91 (2007) 315–329.

[16] C. Peike, S. Hoffmann, P. Hülsmann, B. Thaidigsmann, K. Weiβ, M. Koehl, P. Bentz, Origin of damp-heat induced cell degradation, Solar Energy Materials and Solar Cells 116 (2013) 49–54.

[17] A. Kraft, L. Labusch, T. Ensslen, I. Dürr, J. Bartsch, M. Glatthaar, S. Glunz, H. Reinecke, Investigation of acetic acid corrosion impact on printed solar cell contacts, IEEE Journal of Photovoltaics 5 (2015) 736–743.

[18] N. Iqbal, D. J. Colvin, E. J. Schneller, T. S. Sakthivel, R. Ristau, B. D. Huey, X. Ben, J.-N. Jaubert, A. J. Curran, M. Wang, et al., Characterization of front contact degradation in monocrystalline and multicrystalline silicon photovoltaic modules following damp heat exposure, Solar Energy Materials and Solar Cells 235 (2022) 111468.

[19] S. Jiang, K. Wang, H. Zhang, Y. Ding, Q. Yu, Encapsulation of pv modules using ethylene vinyl acetate copolymer as the encapsulant, Macromolecular Reaction Engineering 9 (2015) 522–529.

[20] M. A. Green, The passivated emitter and rear cell (perc): From conception to mass production, Solar Energy Materials and Solar Cells 143 (2015) 190–197.

[21] A. Blakers, Development of the perc solar cell, IEEE Journal of Photovoltaics 9 (2019) 629–635.

[22] K. R. Mikeska, M. Lu, W. Liao, Tellurium-based screen-printable conductor metallizations for crystalline silicon solar cells, Progress in Photovoltaics: Research and Applications 27 (2019) 1071–1080.

[23] N. Iqbal, M. Li, K. Mikeska, M. Lu, T. S. Sakthivel, S. Seal, K. O. Davis, Impact of acetic acid exposure on the screen-printed tellurite-based silver contacts, in: 2021 IEEE 48th Photovoltaic Specialists Conference (PVSC), IEEE, 2021, pp. 0382–0386.

[24] T. Dullweber, C. Kranz, R. Peibst, U. Baumann, H. Hannebauer, A. Fülle, S. Steckemetz, T. Weber, M. Kutzer, M. Müller, et al., Perc+: industrial perc solar cells with rear al grid enabling bifaciality and reduced al paste consumption, Progress in Photovoltaics: Research and Applications 24 (2016) 1487–1498.

[25] S. Joonwichien, S. Utsunomiya, Y. Kida, M. Moriya, K. Shirasawa, H. Takato, Improved rear local contact formation using al paste containing si for industrial perc solar cell, IEEE Journal of Photovoltaics 8 (2017) 54–58.

[26] N. Balaji, D. Lai, V. Shanmugam, P. K. Basu, A. Khanna, S. Duttagupta, A. G. Aberle, Pathways for efficiency improvements of industrial perc silicon solar cells, Solar Energy 214 (2021) 101–109.

[27] B. Min, M. Müller, B. Wolpensinger, G. Fischer, P. Palinginis, D. H. Neuhaus, R. Brendel, Impact of local back-surface-field thickness variation on performance of perc solar cells, IEEE Journal of Photovoltaics 11 (2021) 908–913.

[28] S. De Wolf, A. Descoeudres, Z. C. Holman, C. Ballif, High-efficiency Silicon Heterojunction Solar Cells: A Review, Green 2 (2012). doi:10.1515/green-2011-0018.

[29] G. A. Armin, B. B. Matthew, H. Bram, M. Thomas, Industrial silicon wafer solar cells – status and trends, Green 2 (2012). doi:10.1515/green-2012-0007.

[30] J. Karas, A. Sinha, V. S. P. Buddha, F. Li, F. Moghadam, G. Tamizh-Mani, S. Bowden, A. Augusto, Damp heat induced degradation of silicon heterojunction solar cells with cu-plated contacts, IEEE Journal of Photovoltaics 10 (2019) 153–158.

[31] W. Liu, L. Zhang, X. Yang, J. Shi, L. Yan, L. Xu, Z. Wu, R. Chen, J. Peng, J. Kang, et al., Damp-heat-stable, high-efficiency, industrial-size silicon heterojunction solar cells, Joule 4 (2020) 913–927.

[32] A. M. Jeffries, T. Nietzold, L. T. Schelhas, M. I. Bertoni, Corrosion of novel reactive silver ink and commercial silver-based metallizations in diluted acetic acid, Solar Energy Materials and Solar Cells 223 (2021) 110900.

[33] F. Feldmann, M. Bivour, C. Reichel, M. Hermle, S. W. Glunz, Passivated rear contacts for high-efficiency n-type si solar cells providing high interface passivation quality and excellent transport characteristics, Solar energy materials and solar cells 120 (2014) 270–274.

[34] A. Richter, J. Benick, F. Feldmann, A. Fell, M. Hermle, S. W. Glunz, n-type si solar cells with passivating electron contact: Identifying sources for efficiency limitations by wafer thickness and resistivity variation, Solar Energy Materials and Solar Cells 173 (2017) 96–105.

[35] J. F. Mousumi, H. Ali, G. Gregory, C. Nunez, K. Provancha, S. Seren, H. Zunft, K. O. Davis, Phosphorus-doped polysilicon passivating contacts deposited by atmospheric pressure chemical vapor deposition, Journal of Physics D: Applied Physics 54 (2021) 384003.

[36] J. F. Mousumi, G. Gregory, J. P. Ganesan, C. Nunez, K. Provancha, S. Seren, H. Zunft, T. Jurca, P. Banerjee, A. Kar, et al., Process–structure–properties relationships of passivating, electron-selective contacts formed by atmospheric pressure chemical vapor deposition of phosphorus-doped polysilicon, physica status solidi (RRL)–Rapid Research Letters (2022) 2100639.

[37] S. Theingi, W. Nemeth, K. Chen, M. Page, P. Stradins, D. L. Young, Accelerated reliability tests of n+ and p+ poly-si passivated contacts, Solar Energy Materials and Solar Cells 236 (2022) 111469.

[38] G. Gregory, M. Li, A. Gabor, A. Anselmo, Z. Yang, H. Ali, N. Iqbal, K. Davis, Nondestructive contact resistivity measurements on solar cells using the circular transmission line method, IEEE Journal of Photovoltaics 9 (2019) 1800–1805.

[39] G. C. Eder, G. Voronko, Y. Knausz, M. Berger, Permeation of water vapour oxygen and acetic acid through pv-backsheets: correlation with material properties and ageing induced changes, EU PVSEC (2015).

[40] S. Marais, E. Bureau, F. Gouanve, E. B. Salem, Y. Hirata, A. Andrio, C. Cabot, H. Atmani, Transport of water and gases through eva/pvc blend films—permeation and dsc investigations, Polymer testing 23 (2004) 475–486.

[41] R. Sinton, A. Cuevas, A Quasi-Steady-State Open-Circuit Voltage Method for Solar Cell Characterization, in: 16th European Photovoltaic Solar Energy Conference, Glasgow, Scotland, 2000, pp. 1152–1155.

[42] M. Li, N. Iqbal, Z. Yang, X. Lin, N. K. Pannaci, C. Avalos, T. Shaw, K. Davis, et al., A comprehensive evaluation of contact recombination and contact resistivity losses in industrial silicon solar cells, IEEE Journal of Photovoltaics 10 (2020) 1277–1282.

[43] N. Iqbal, M. Li, G. Gregory, S. Dahal, S. Bowden, K. O. Davis, Recombination and resistive losses of transferred foil contacts for silicon heterojunction solar cells, physica status solidi (RRL)–Rapid Research Letters 14 (2020) 2000368.

[44] E. J. Schneller, K. Öğütman, S. Guo, W. V. Schoenfeld, K. O. Davis, Crystalline silicon device loss analysis through spatially resolved quantum efficiency measurements, IEEE Journal of Photovoltaics 7 (2017) 957–965.

[45] S. Guo, G. Gregory, A. M. Gabor, W. V. Schoenfeld, K. O. Davis, Detailed investigation of tlm contact resistance measurements on crystalline silicon solar cells, Solar Energy 151 (2017) 163–172.

[46] J. Wong, J. W. Ho, D. Inns, F. Fruhauf, Luminescence Image Analysis Using Finite-Element Models: Finished Solar Cell Analysis, IEEE Journal of Photovoltaics 10 (2020) 159–165. doi:10.1109/JPHOTOV.2019.2942812.

[47] M. Bahl, R. Watson, K. Irgolic, X-ray photoemission studies of tellurium and some of its compounds, The Journal of Chemical Physics 66 (1977) 5526–5535.

[48] T. Semba, New corrosion mechanism observed at ag/al metallization of n-type bifacial solar cells, in: 2020 47th IEEE Photovoltaic Specialists Conference (PVSC), IEEE, 2020, pp. 0850–0853.

[49] A. S. Ionkin, B. M. Fish, Z. R. Li, M. Lewittes, P. D. Soper, J. G. Pepin, A. F. Carroll, Screen-printable silver pastes with metallic nano-zinc and nano-zinc alloys for crystalline silicon photovoltaic cells, ACS Applied Materials & Interfaces 3 (2011) 606–611.

[50] P. Kumar, M. Pfeffer, B. Willsch, O. Eibl, Contact formation of front side metallization in p-type, single crystalline si solar cells: Microstructure, temperature dependent series resistance and percolation model, Solar Energy Materials and Solar Cells 145 (2016) 358–367.

[51] E. A. Gaulding, J. S. Mangum, S. W. Johnston, C.-S. Jiang, H. Moutinho, M. J. Reed, J. A. Rand, R. Flottemesch, T. J. Silverman, M. G. Deceglie, Differences in printed contacts lead to susceptibility of silicon cells to series resistance degradation, IEEE Journal of Photovoltaics (2022).